Department of Physics and Astronomy
University of Heidelberg

Bachelor Thesis in Physics
submitted by

Christoph Sünderhauf

born in Darmstadt (Germany)

2014

Quantum Reflection in Time and Space

(revised version)

This Bachelor Thesis has been carried out by Christoph Sünderhauf at the
Institute for Theoretical Physics in Heidelberg
under the supervision of
Dr. Sandro Wimberger

Quantum Reflection in Time and Space

The reflection of a particle from an attractive potential is called quantum reflection and has no classical counterpart. It is possible to use a numeric approach that integrates the time-dependent Schrödinger equation in one dimension to study quantum reflection at a surface. This project uses the approach to analyse the time course of quantum reflection and develops a model to describe it. It is shown that the time behaviour of the reflection process is highly dependent on the shape of the incident particle's wave function. Furthermore, differences between quantum and classical reflection at the surface are investigated. As experiments show that one-dimensional modelling of quantum reflection is insufficient, an extension of the approach to two dimensions is sought and assessed. Computational requirements for practically using the proposed extension are extrapolated.

Quantenreflexion in Zeit und Raum

Die Reflexion eines Teilchens an einem attraktiven Potential wird Quantenreflexion genannt und hat kein klassisches Gegenstück. Mit einem numerischen Ansatz, in dem die zeitabhängige Schrödingergleichung in einer Dimension integriert wird, ist es möglich Quantenreflexion an einer Oberfläche zu untersuchen. Dieses Projekt verwendet den Ansatz, um den zeitlichen Verlauf von Quantenreflexion zu analysieren und entwickelt ein Modell für dessen Beschreibung. Es wird gezeigt, dass das zeitliche Verhalten des Reflexionsprozesses stark von der Gestalt des Wellenpakets des einfallenden Teilchens abhängig ist. Darüber hinaus werden Unterschiede zwischen Quanten- und klassischer Reflexion an der Oberfläche untersucht. Weil Experimente zeigen, dass eindimensionale Modellierung von Quantenreflexion ungenügend ist, wird eine zweidimensionale Erweiterung des Ansatzes gesucht und bewertet. Die benötigte Rechenleistung für die praktische Umsetzung der vorgeschlagenen Erweiterung wird extrapoliert.

Contents

1 Introduction **6**

2 Background **7**

3 Results **10**

3.1 Two-dimensional numeric approach 10

3.1.1 Theoretical considerations 10

3.1.2 Practical considerations 12

3.2 Time behaviour of reflection 16

3.2.1 Physical and numeric background 17

3.2.2 Shape of reflectivity 18

3.2.3 Quantum and classical reflection in comparison 24

3.2.4 Experimentally isolating quantum and classical reflection 25

4 Conclusion and Perspectives **32**

1 Introduction

The phenomenon quantum reflection denotes the reflection from an attractive potential. Since there is no classical counterpart to this quantum mechanical effect, it might seem quite surprising. But yet it is so fundamental that a simple example is usually covered in introductory lectures to quantum mechanics [1]: A particle being reflected at a potential step downwards is an example of quantum reflection. Nevertheless, this phenomenon seems not to be known very widely [2].

Quantum reflection can be observed in the interaction between an atom and a surface because the interaction potential has an attractive regime [3]. Quantum reflectivity strongly depends on the energy of the incoming particle. In order to measure effects due to quantum reflection, very slow particles have to be used. Experimentally, this is achieved by tilting the atomic beam with respect to the surface, such that the normal component of the velocity is small.

A one-dimensional numerical scheme for calculation of quantum reflection effects is available [4]. However, in experiments with non-homogeneous, periodic surfaces, quantum reflectivity depends on the incident angle with respect to the periodicity of the surface [5]. Thus, a one-dimensional approach to quantum reflection is insufficient and a possible two-dimensional extension as suggested in this project is of interest.

A basic question which seems interesting is the time course and swiftness of quantum reflection. Therefore, the reflection process is analysed in this project. A surface potential has a repulsive regime in addition to the attractive regime. Apart from quantum reflection in the attractive regime, an incident particle can also be classically reflected in the repulsive regime. Calculations that motivate an experimental measurement of the expected delay between classical and quantum reflection are carried out.

2 Background

The interaction between atom and surface is described by the surface potential

$$V(x) = Ae^{-Kx} - \frac{C_3}{(x - x_0)^3} \tag{1}$$

with coefficients A, K, C_3 and x_0 dependent on the materials in question [6, 7].

Methods developed by B. Herwerth [4, 8] were employed to study quantum reflection numerically in one dimension. In a nutshell, the wave function of the particle is sampled at several grid points with spacing dx and propagated using a Crank-Nichelson scheme [9]. This involves solving the equation

$$\left(1 + \frac{iHdt}{2\hbar}\right)\psi_{t+dt} = \left(1 - \frac{iHdt}{2\hbar}\right)\psi_t \tag{2}$$

for every time step dt. The derivative in the Hamiltonian

$$H = V(x) - \frac{\hbar^2}{2m}\frac{\partial^2}{\partial x^2} \tag{3}$$

is discretised using a three-point approximation [10]

$$\frac{\partial^2}{\partial x^2}\psi(x) \approx \frac{1}{(dx)^2}\psi(x - dx) - \frac{2}{(dx)^2}\psi(x) + \frac{1}{(dx)^2}\psi(x + dx). \tag{4}$$

This leads to the matrix on the left hand side of Eq. (2) being tridiagonal. An efficient algorithm for tridiagonal matrices [9] was then used to solve the equation.

In order to study quantum reflection opposed to reflection at the full potential which includes classical reflection, only the absorptive part

$$V(x) = -\frac{C_3}{x^3}. \tag{5}$$

of the potential is used. However, the potential's singularity at $x = 0$ leads to numeric issues. Since the potential becomes very deep, the equally spaced grid is insufficient and artificial reflections of the wave function occur. This can be circumvented by introducing a cut off point x_{stop}. The potential is cut off at x_{stop} and parabolically continued to a linear regime. See Fig. 1 for an illustration of the potential. To avoid reflections at the edge of the numeric box, an absorptive filter smoothly multiplying the wave function to zero is applied.

An initial Gaussian wave packet with velocity $v < 0$ is propagated into the potential.

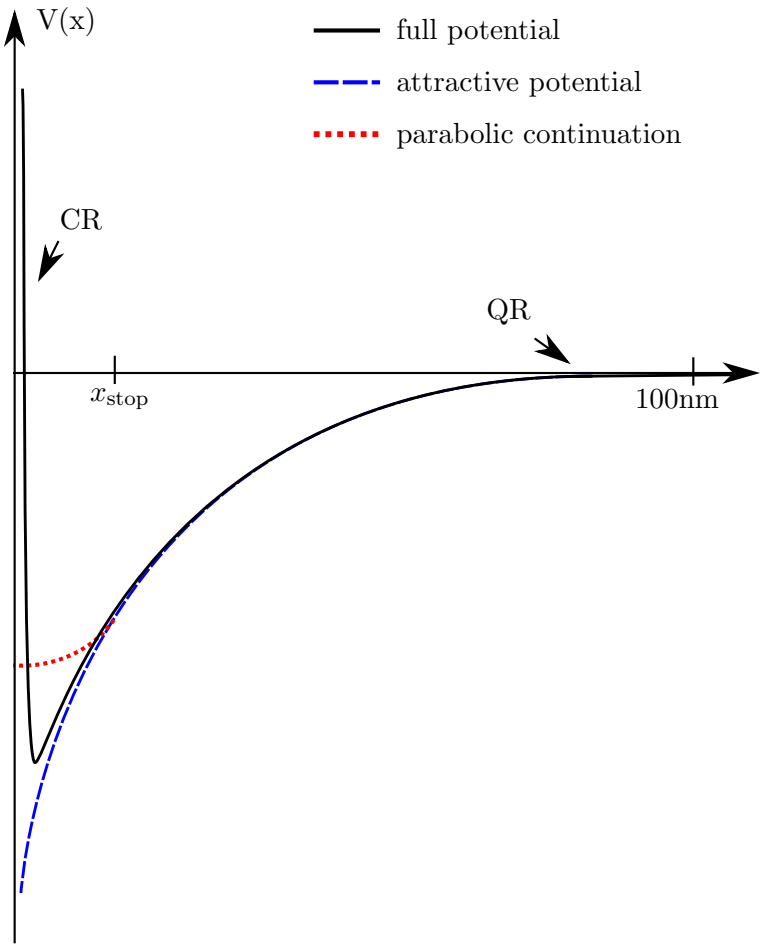

Figure 1: Illustration of the potentials mentioned in the text. Classical reflection takes place at the repulsive regime of the potential. Quantum reflection occurs in the region where the potential depth equals the incoming particle's energy (see [11], p. 16). Hence, quantum reflection is expected to be similiar for all three potentials shown.

After allowing enough time for reflection, quantum reflectivity R can be calculated from the reflected wave function $\psi_{t_{\text{final}}}$. This can be done both in coordinate space $R = \int_{x_{\min}}^{\infty} |\psi_{t_{\text{final}}}(x)|^2 dx$ and momentum space $R = \int_0^{\infty} |\psi_{t_{\text{final}}}(p)|^2 dp$. The lower integration bound $x_{\min} > 0$ is chosen well out of the potential, ensuring that only reflected parts of the wave function are taken into account. The lower bound of the integral in momentum space must be zero, because the incoming particle has negative momentum and the (elastically reflected) outgoing particle will have positive momentum. For calculation of R in momentum space to succeed, it is important that the width Δp is sufficiently small. Otherwise, the wave packet is so wide that it always contains both negative and positive momentum components, no matter whether the average momentum is positive or negative.

The determined reflectivity is dependent on the choice of the potential cut off point x_{stop}. It shows a periodic behaviour in x_{stop} which converges as $x_{\text{stop}} \to 0$. Reflectivity for the physical potential without cut off can then be extrapolated as $x_{\text{stop}} \to 0$.

This method of numerically propagating the wave packet can be extended to two dimensions using a split operator technique if the potential used is separable (see [12], pp. 497f.), i.e. $V(x, y) = V_x(x) + V_y(y)$. However, the physical potentials in question are not separable and a different extension must be sought.

3 Results

3.1 Two-dimensional numeric approach

3.1.1 Theoretical considerations

Generalisation of the one dimensional scheme onto a two dimensional $n \times m$ grid ($m < n$) with spacings dx and dy is possible. On such a grid, $n \cdot m$ values of $\psi(x, y)$ have to be stored. The Hamiltonian H then is a $(n \cdot m) \times (n \cdot m)$ matrix acting on this representation of ψ. There are multiple possible orders in which the grid can be traversed and in which the values of ψ are saved, each described by a one-to-one mapping

$$f : \{1, \ldots, n \cdot m\} \to \{1, \ldots, n\} \times \{1, \ldots, m\}. \tag{6}$$

Examples of possible mappings f are shown in Figure 2.

As in the one dimensional case, the equation

$$\left(1 + iH\frac{dt}{2\hbar}\right)\psi_{t+dt} = \left(1 - iH\frac{dt}{2\hbar}\right)\psi_t \tag{7}$$

needs to be solved. However, now the matrix on the left hand side, which we shall call M, is not tridiagonal. It is still symmetric, so it was decided to calculate the LL^t decomposition which makes use of the symmetry. This then allows efficient back substitution to obtain ψ_{t+dt} (see [9], p. 100). A close look at the algorithm reveals that for a banded matrix with bandwidth b, the number of computation steps needed is $n \cdot m \cdot b^2$, at least in the highest order. Therefore, it is reasonable to choose a mapping f which results in M having low bandwidth.

The derivatives in the Hamiltonian $H = V(x, y) - \frac{\hbar^2}{2m}\frac{\partial^2}{\partial x^2} - \frac{\hbar^2}{2m}\frac{\partial^2}{\partial y^2}$ can be expanded with the three point approximation as in the one-dimensional case (Eq. (4)), separately for each spatial direction. Then M has the following non-zero elements: diagonals (Eq. (8))

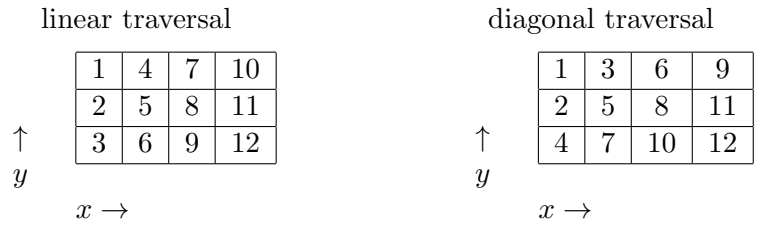

Figure 2: Examples of two different mappings f for a 4×3 grid. The numbers indicate the index of the grid boxes.

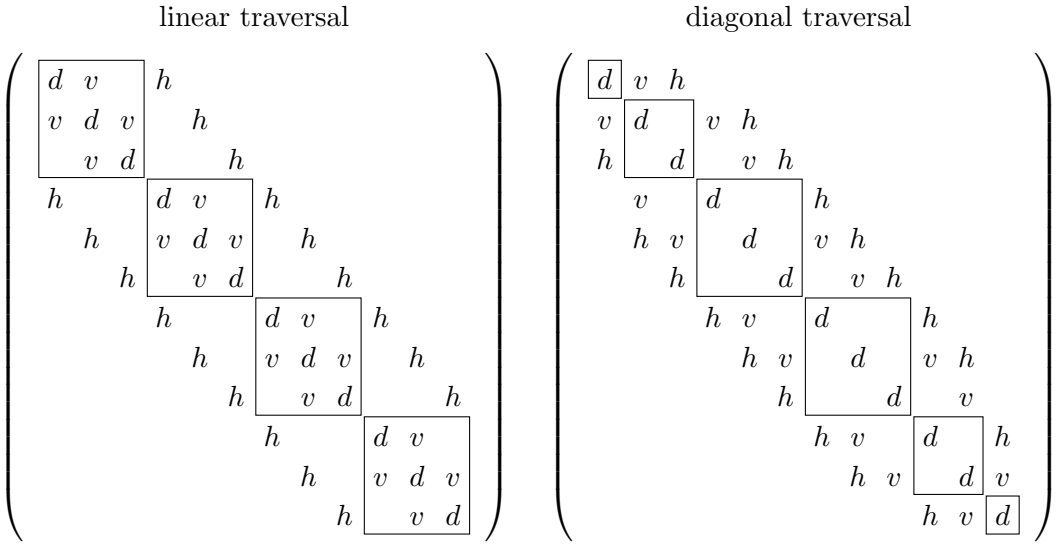

Figure 3: Examples of the matrix $M = 1 + iH\frac{dt}{2\hbar}$ for the two mappings f from Fig. 2. The non-zero components are given as d for the diagonals (Eq. (8)) and h, v for the terms resulting from horizontally (Eq. (9)) and vertically (Eq. (10)) adjacent grid boxes, respectively. In the linear traversal, the matrix blocks indicate one column of grid boxes each. In the diagonal traversal, they indicate one diagonal each.

and off-diagonals where the grid box $f(j)$ is adjacent to $f(k)$ in x-direction (Eq. (9)) or y-direction (Eq. (10)).

$$M_{j,j} = 1 + V(f(j))\, i\frac{dt}{2\hbar} + i\frac{2\hbar^2}{2m(dx)^2}\frac{dt}{2\hbar} + i\frac{2\hbar^2}{2m(dy)^2}\frac{dt}{2\hbar} \tag{8}$$

$$M_{j,k} = -i\frac{\hbar^2}{2m(dx)^2}\frac{dt}{2\hbar} \tag{9}$$

$$M_{j,k} = -i\frac{\hbar^2}{2m(dy)^2}\frac{dt}{2\hbar} \tag{10}$$

Structures of M for the two mappings f considered as an example are shown in Figure 3.

In the following, an intuitive method which yields lower limits for the bandwidth b is developed. Next, this is used to show $b \geq m$ if m is small enough such that $n \geq 2m - 1$. Having shown that a bandwidth lower than m is not possible, f from the first example in Figure 2 can be used in computations. This common approach of traversing the grid column-by-column results in a bandwidth m for every grid size and a rather simple matrix M.

For a fixed mapping f, let j be an arbitrary index, $1 < j < n \cdot m$. Colour all of the grid boxes $f(1), f(2), \ldots, f(j)$ grey. Now consider the number p of non-coloured (spatial) neighbour boxes of these grey boxes. Let k be the highest index of any of these non-coloured neighbours. Then $k \geq j + p$. Since $f(k)$ is a neighbour to the grey-coloured boxes, there is a box $f(j')$ with $j' \leq j$ that is adjacent to $f(k)$. This means that the matrix element $M_{k,j'}$ is non-zero. Hence,

$$b \geq k - j' \geq (j + p) - (j) = p. \tag{11}$$

The number of neighbours p specifies a lower limit for the bandwidth b.

Now we need to use this neighbour counting method to show $b \geq m$ for $n \geq 2m - 1$. Subsequently, we will use the argument that a row (column) partially coloured contains at least one horizontal (vertical) neighbour box. Care has to be taken to use only either rows or columns in this argument at any one time because otherwise neighbours might be counted twice. Assume we had a mapping f with a bandwidth lower than m and choose $j = m^2$, i.e. colour the first m^2 grid boxes.

There is no completely coloured row with n coloured grid boxes: If there was, consider the row with the least number $k \geq 0$ of coloured grid boxes. This implies at least $n - k$ partially coloured columns hence neighbours. See Fig. 4 for an example. Apart from our row with n coloured grid boxes, there are $m - 1$ further rows and thus distributing the m^2 coloured boxes yields $k \leq (m^2 - n)/(m - 1)$. Then the number of neighbours p is

$$p \geq n - k \geq n - \frac{m^2 - n}{m - 1} = \frac{nm - m^2}{m - 1} \geq \frac{(2m - 1)m - m^2}{m - 1} = m \tag{12}$$

and the bandwidth is at least m.

Next, consider the number m' of rows that contain coloured boxes. If $m' = m$ we are finished, because none of the rows is completely coloured and that yields at least m horizontal neighbours, one in each row. If however $m' < m$ there is one completely uncoloured row. Also, there must be $n' > m$ columns with coloured boxes, because m' rows and n' columns can accommodate at most $m'n'$ boxes and there are m^2 coloured boxes in total. These n' columns are partially coloured due to the one completely uncoloured row and yield $n' > m$ vertical neighbours.

3.1.2 Practical considerations

The suitability of this numerical scheme concerning computational resources needed was assessed and dependence of time and memory consumption on grid size $n \times m = 2^{n_x} \times 2^{n_y}$

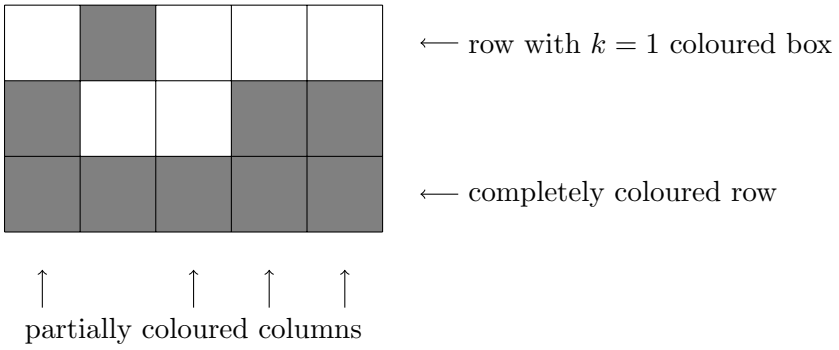

Figure 4: In this example with $n = 5$, $m = 3$, the bottom row is completely coloured. The top row has the least coloured boxes; one, hence $k = 1$. This implies that there are at least $n - k = 4$ partially coloured columns as indicated. Note that the second column is not counted because it may well be fully coloured, as we only have the information that the last row is completely coloured and the first row has one coloured box.

measured.

In the highest order, the 2^{n_y} bands of L contain $2^{n_y} \cdot 2^{n_x+n_y}$ numbers. Hence, incorporating a static offset for components independent of n_x and n_y, memory usage is expected to be described by

$$f(n_x, n_y) = A + B \cdot C^{n_x+2n_y} \tag{13}$$

with suitable constants A, B and $C = 2$. Memory usage of a program performing the decomposition was measured for several grid sizes and is shown in Fig. 5. The deviations at $n_y \leq 3$ are explained by the fact that Eq. (13) does not take into account lower orders which are more significant for small n_y. A fit to the data results in $C \approx 2$ and confirms that Eq. (13) describes memory usage.

The second significant indicator for the scheme's performance is computation time. As mentioned in section 3.1.1, about nmb^2 computation steps are needed for bandwidth b. As $b = m$ has been chosen as the optimum, required time is estimated as $2^{n_x+3n_y}$, at the highest order. Hence, the relation

$$f(n_x, n_y) = A + B \cdot C^{n_x+3n_y} \tag{14}$$

with $C = 2$ is expected for computation time. Since start up and initialisation of the program proved to be negligible, $A = 0$ was fixed. Time needed for performing the decomposition (user time) was measured for several pairs (n_x, n_y) of parameters. Contrary to memory, the measured computation time will vary depending on system

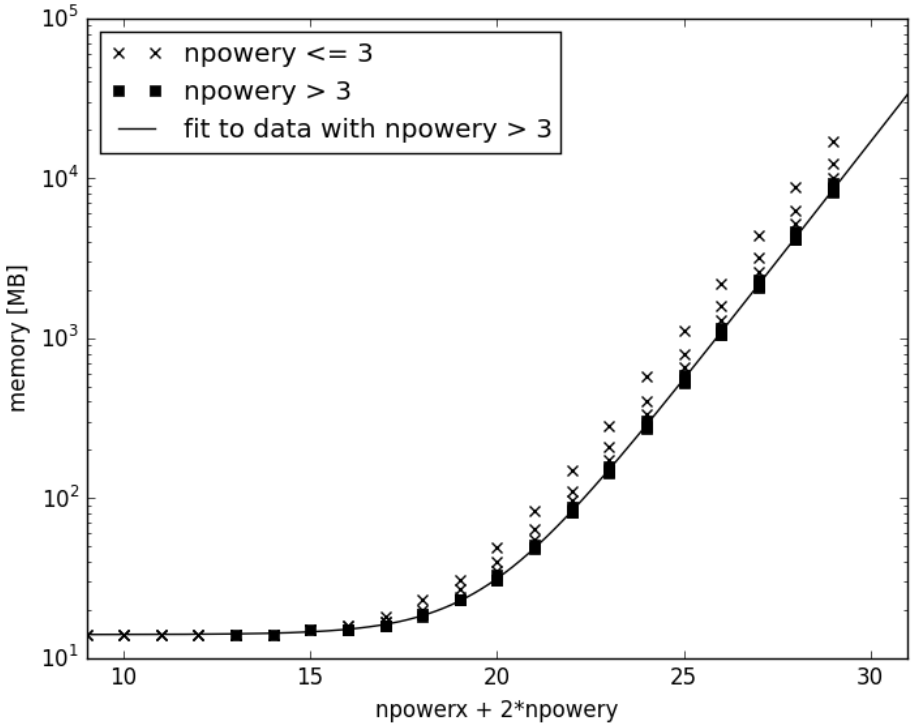

Figure 5: Memory needed for banded storage of LL^t decomposition. Memory usage of the program was measured for all $n_y < n_x$, $n_x + 2n_y \leq 29$. Parameters of $f(n_x, n_y) = A + B \cdot C^{n_x+2n_y}$ were determined as $A \approx 14.02\,\mathrm{MB}, B \approx 1.86 \cdot 10^{-5}\,\mathrm{MB}$, and $C \approx 1.99$.

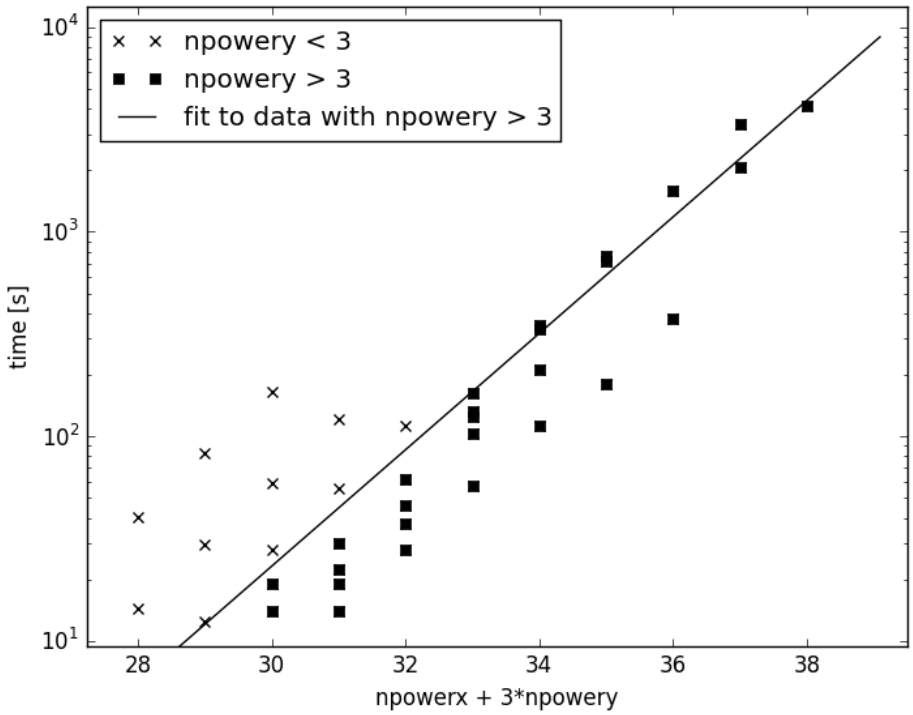

Figure 6: Computation time of LL^t decomposition. Computation time was measured twice and averaged for each $n_y < n_x$, $n_x + 2n_y \leq 29$. Parameters of $f(n_x, n_y) = B \cdot C^{n_x+3n_y}$ were determined as $B \approx 6.82 \cdot 10^{-8}$ s and $C \approx 1.92$.

load. Therefore, it was measured twice for each pair (n_x, n_y) and the average plotted in Fig. 6. The fit results in $C \approx 2$ and confirms Eq. (14).

Using the above data, resources needed for a two dimensional propagation can be estimated. In one dimension, reasonable grid sizes are 2^{16} grid points per 8μm [4]. On the assumption that this spacing is also reasonable in the two-dimensional scheme, a $4\mu\text{m} \times 2\mu\text{m}$ grid ($n_x = 15, n_y = 14$) would need about 130 terrabytes of memory and about 35 years for an LL^t decomposition. Clearly this is not feasible.

What may be possible is using periodic boundary conditions along the y-direction. Then the grid height can be small and n_y, which effects resources stronger than n_x, lower. Using periodic boundary conditions in the y-direction still makes it possible to construct a matrix M with bandwidth $m = 2^{n_y}$. In fact, linear traversal as in Fig. 2 stays possible. Because of periodic boundary conditions, there are more vertically adjacent grid boxes and the free components in the first off-diagonal of M (see Fig. 3) will be filled with v. Considerations that showed a bandwidth lower than m cannot be achieved stay valid, because only lower bounds of the number of neighbours were needed and periodic boundary conditions add neighbours.

A $2\mu\text{m} \times 0.0625\mu\text{m}$ grid ($n_x = 14, n_y = 9$) needs about 67 gigabytes and 9 hours. If a time dependent potential shall be used, the LL^t decomposition has to be repeated every few time steps. Then LL^t decomposition should be the dominating factor as the multiplication on the right hand side of Eq. (7) and back substitution is significantly faster. Alternatively, in the case of a potential periodic in time, the decomposition can be saved for multiple times which improves computation time at the cost of memory. In conclusion, this method for two-dimensional propagation in a time-dependent potential is presently not viable.

3.2 Time behaviour of reflection

The reflectivity

$$R = \int_0^\infty |\psi_t(p)|^2 dp \tag{15}$$

can be measured not just in the limit $t \to \infty$ as explained in section 2 but at multiple times t. This was done by performing a fast Fourier transformation [9] of the wave function $\psi(x)$ every few time steps and numerically integrating in the momentum domain.

The resulting time behaviour $R(t)$ was analysed using the SciPy libraries for Python [13] and proved qualitatively independent of the precise physical (and numeric) parameters of the system, such as velocity and width of incoming particle. An example of the time behaviour is shown in Fig. 7. It exhibits two important features which will be discussed

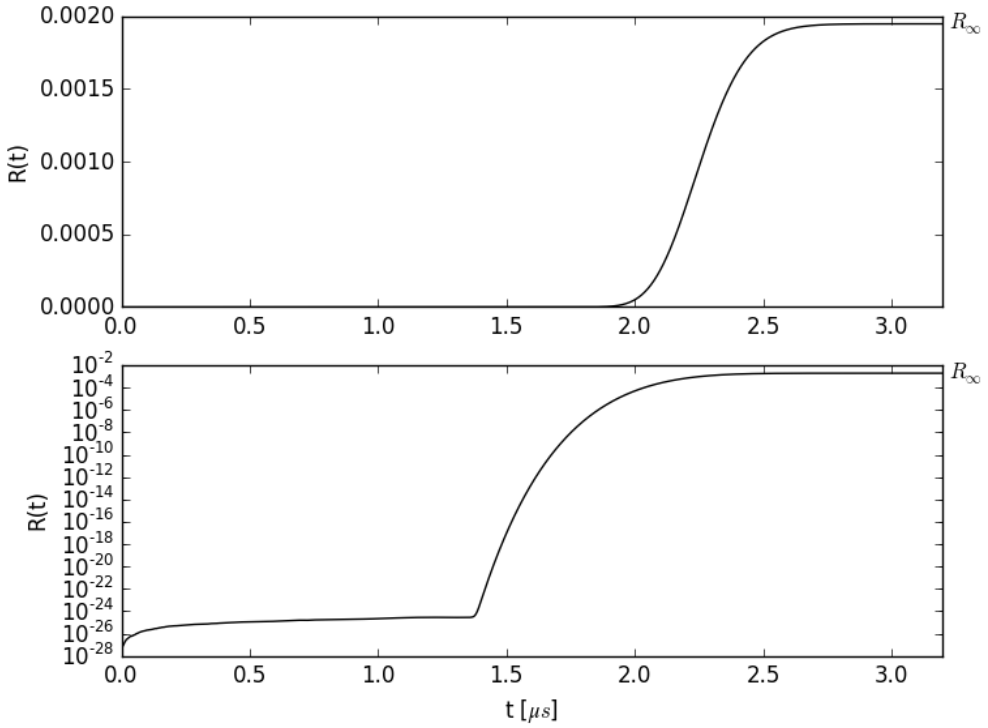

Figure 7: Typical example of $R(t)$ in both logarithmic and linear scale. It is clearly visible that R saturates at the final reflectivity R_∞ as $t \to \infty$.

hereafter.

3.2.1 Physical and numeric background

First, a saturation of the reflectivity at R_∞ as $t \to \infty$ is seen in both logarithmic and linear plot (Fig. 7). Physically, this is due to the reflection process finishing. All of the incoming particle has either been reflected or transmitted beyond the quantum reflection point. Quantum reflectivity is not one, hence the final reflectivity is lower than one. The time course $R(t)$ of classical reflection however should saturate at $R_\infty = 1$, because transmission through a (sufficiently high) classical barrier does not happen. Therefore, a unitarity check of the numerical method was carried out by computing $R(t)$ for classical reflection and successfully confirming $R(t \to \infty) = 1$.

The other feature is the abrupt pick-up of R after the constant regime at short t, which is only visible in the logarithmic scale (Fig. 7). Both the constant regime and abrupt pick-up visible are due to background.

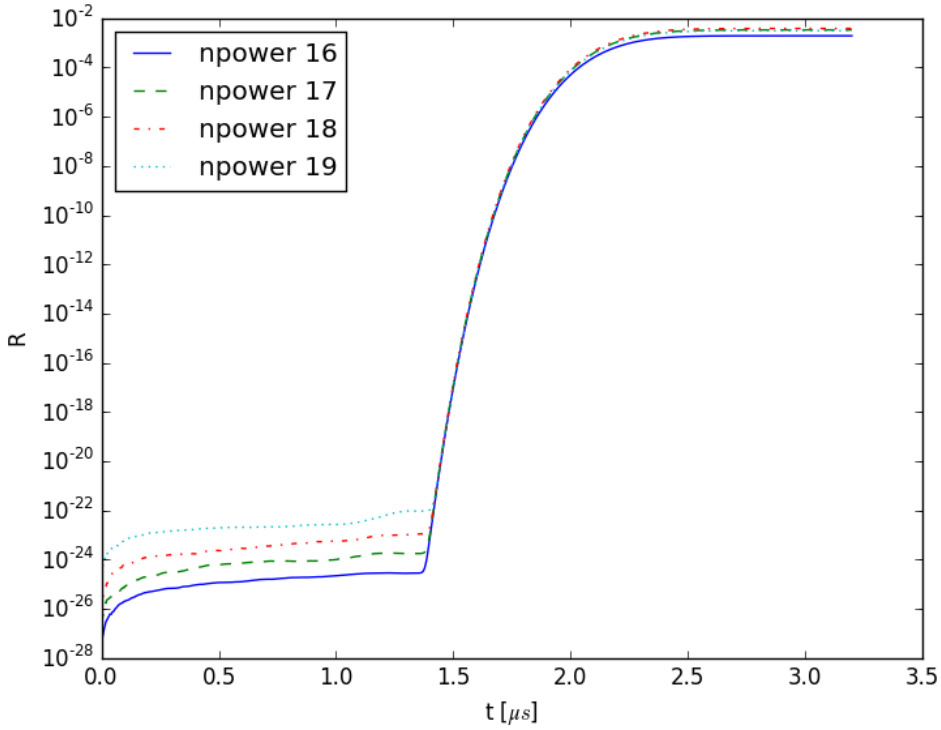

Figure 8: $R(t)$ for different numbers of grid points 2^{npower}. The background visible at small t is dependent on numeric parameters.

Physically, the initial Gaussian wave packet already contains a small amount of positive momentum, even though this will be minute in the case of mean momentum $p_0 = -2\text{m/s} \cdot 5 \cdot 10^{-27}\text{kg} = -10^{-26}\text{kg m/s}$ and width $\Delta p = \hbar/(2 \cdot \Delta x) = \hbar/(2 \cdot 0.08 \cdot 10^{-6}\text{m}) = 6.6 \cdot 10^{-28}\text{kg m/s}$, on the order of $R(t = 0) \approx 4 \cdot 10^{-52}$, which is negligible with respect to the numeric background discussed next. [14]

The dominating effect is numeric background. This is dependent on the numeric parameters chosen, such as the number of grid points as can be seen in Fig. 8. Hence, the rather abrupt pick-up of $R(t)$ and its precise position have no physical meaning. Rather, it indicates that reflectivity has started exceeding the numeric background, becoming visible on the logarithmic plot.

3.2.2 Shape of reflectivity

The time behaviour of $R(t)$ in Fig. 7 looks like an error function. This can be explained physically. The error function is a cumulative integral of the normal distribution. Hence,

the derivative dR/dt resembles a Gaussian function

$$g(t) = A \cdot \exp\left(-B \cdot (t - t_0)^2\right). \tag{16}$$

An advantage of looking at the derivative is that the (approximately constant) background disappears. Eq. (16) is similar to the density of the initial wave packet

$$|\psi(x, t = 0)|^2 = \frac{1}{\sqrt{2\pi}\sigma_0} \exp\left(-\frac{(x - x_0)^2}{2\sigma_0^2}\right) \tag{17}$$

with initial position x_0 and width σ_0.

Quantum reflection predominantly occurs at the position $\tilde{x}$ where the potential depth is the same as the particle's initial energy [5]. The amount dR reflected in a time step dt is directly dependent on the density $|\psi(\tilde{x}, t)|^2$,

$$\frac{dR(t)}{dt} = \tilde{R} \cdot |\psi(\tilde{x}, t)|^2. \tag{18}$$

The reflectivity coefficient $\tilde{R}$ has units m/s and is not identical to $R_\infty = R(t \to \infty)$.

Let us simplify and assume, that the wave packet's evolution till x_0 resembles free propagation. Then we have

$$|\psi(\tilde{x}, t)|^2 = \frac{1}{\sqrt{2\pi}\sigma(t)} \exp\left(-\frac{(\tilde{x} - (x_0 + vt))^2}{2\sigma^2(t)}\right) \tag{19}$$

with time-dependent width (see [1], p. 54)

$$\sigma^2(t) = \sigma_0^2 + \frac{\hbar^2}{4m^2\sigma_0^2} t^2 \tag{20}$$

and initial velocity v. Note that the particle is incident from the right and $v < 0$.

The above must be tested against simulated results. Fig. 9 shows a fit of Eqs. (18) through (20). The fit describes this specific set of data very well. To ensure that quantum reflection generally follows this pattern, fits to simulation results with various simulation parameters v, σ_0 and x_{stop} were performed. Altogether, the fits looked as good as the example in Fig. 9. Fit parameters resulting from these fits are shown in Figs. 10 through 12.

The residuals seen in Fig. 9 do not randomly scatter about zero as would be expected for a statistically limited fit. Indeed, another effect must be taken into account: The reflectivity coefficient $\tilde{R}$ is not constant as assumed in the fit. In fact, reflectivity is

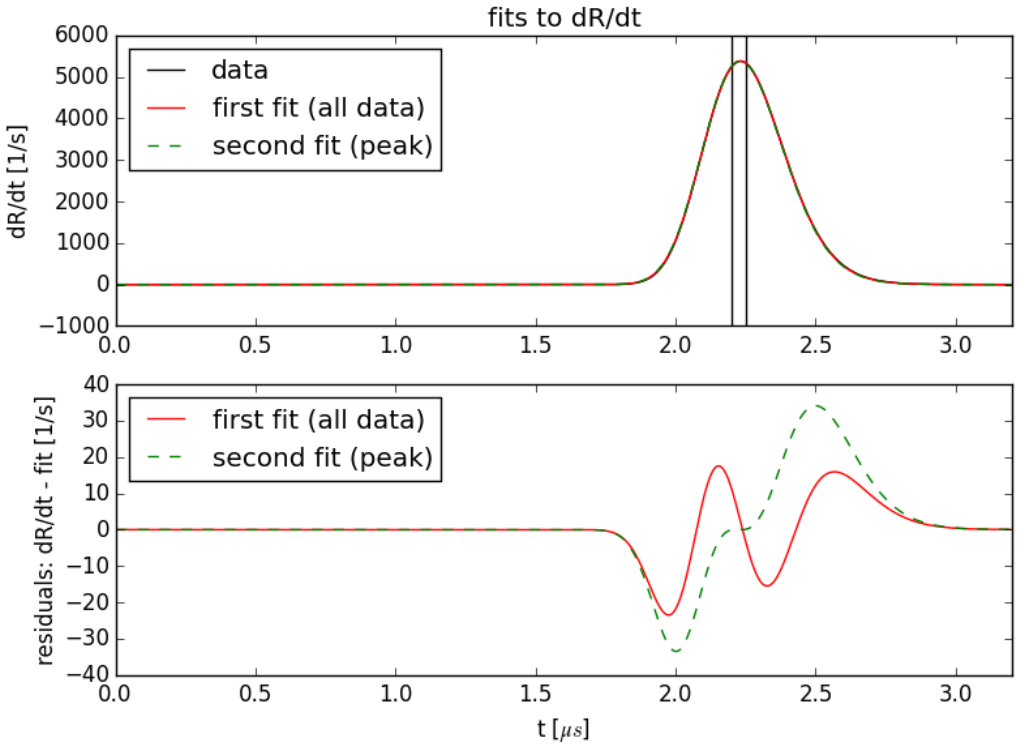

Figure 9: Fits of Eqs. (18) through (20) to $dR(t)/dt$ and corresponding residuals $dR(t)/dt - \mathrm{fit}(t)$. Velocity $v = -2\mathrm{m/s}$ and mass m were fixed to the values used in the numeric simulation. Free parameters obtained with the fit are $\tilde{R}$, σ_0 and $(\tilde{x} - x_0)$. While the first fit uses all data, the second fit only considers data around the peak, indicated by the vertical lines. The non-random residuals are discussed in the text.

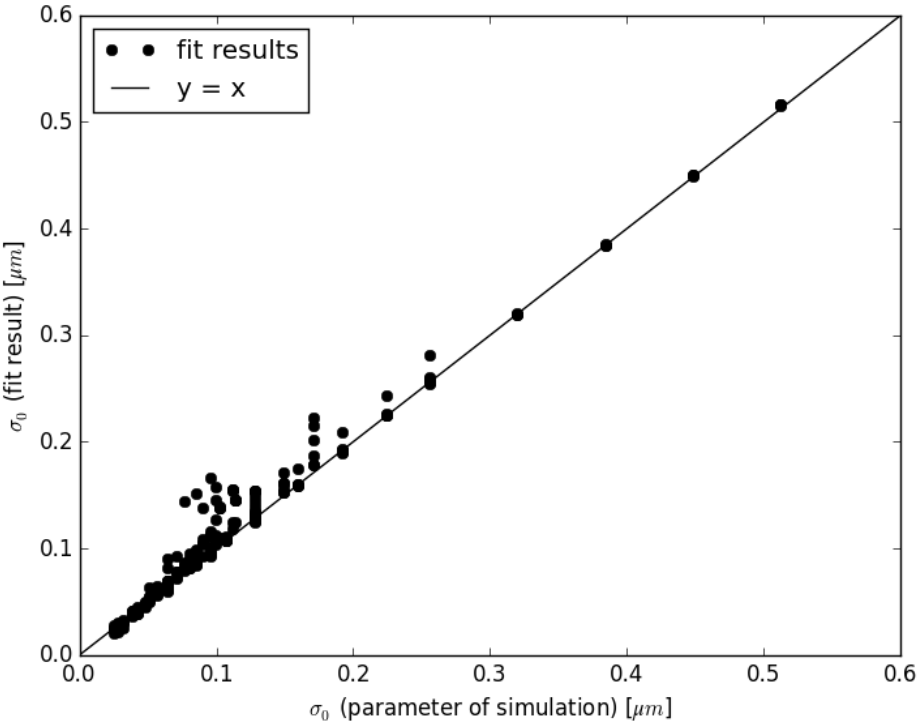

Figure 10: Fit parameter σ_0 plotted against σ_0 used in the numeric simulation. Of course, they are expected to be the same and lie on the identity. For most fit results, this is the case.

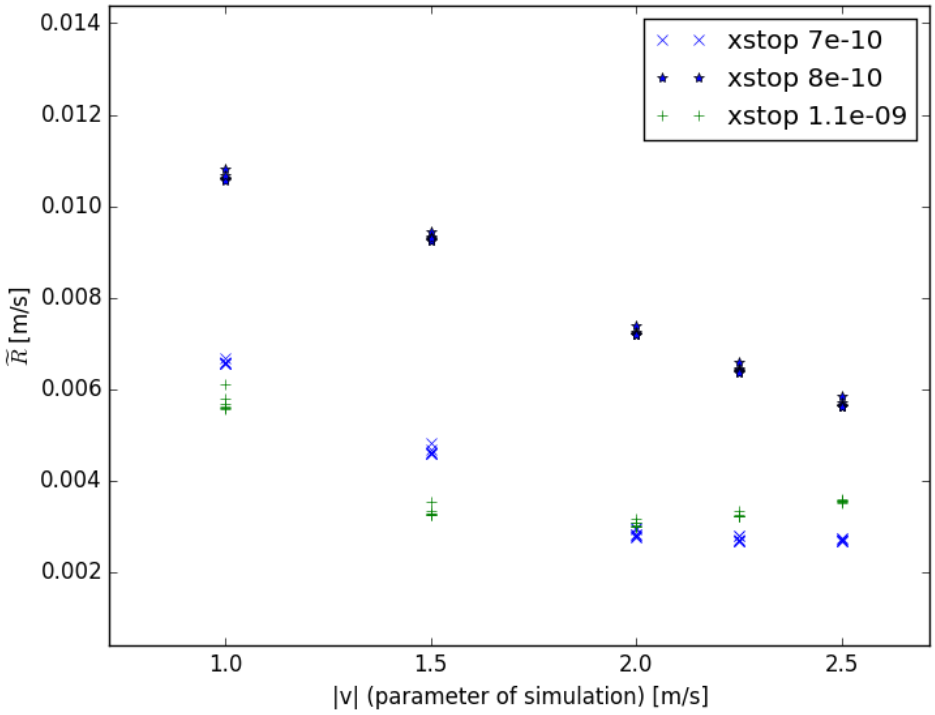

Figure 11: Fit parameter $\tilde{R}$ plotted against $|v|$ used in the numeric simulation. Reflectivity varying with x_{stop} is not surprising [4]. A trend showing higher $\tilde{R}$ for lower velocities is apparent and expected according to Shimizu [3].

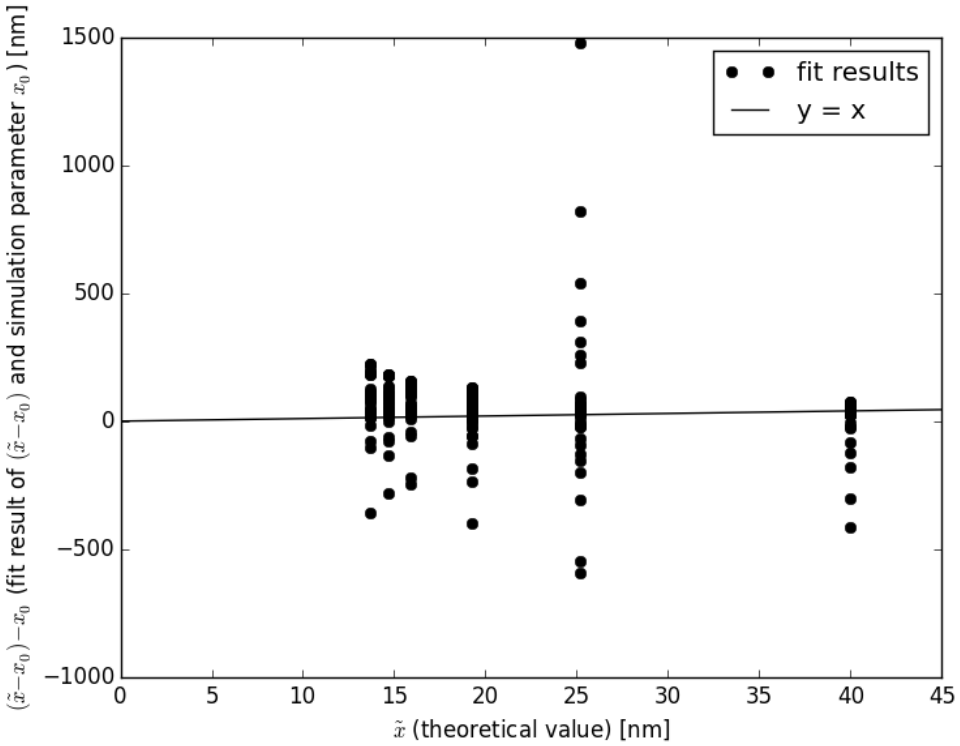

Figure 12: Fit parameter $(\tilde{x}-x_0)$ plus simulation parameter x_0 plotted against theoretical $\tilde{x} = \sqrt[3]{2C_3/(mv^2)}$. The fit parameters are expected to lie on the identity. This is not the case. The model used for the fit is insufficient as is discussed in the text.

strongly dependent on velocity of incident particles. Components of the wave function reaching $\tilde{x}$ first are faster and have a lower $\tilde{R}$ whereas components being reflected later have lower velocity and a higher reflectivity coefficient.

This effect is best seen in the second fit in Fig. 9, which was only optimised against a small region of data near the peak. These components of the wave function can be expected to have the same velocity and hence $\tilde{R}$. The corresponding residuals clearly show that components being reflected first have a lower reflectivity and components reflected later a higher reflectivity. However, at other parameters, the residuals are exactly opposite: above zero before and below zero after the peak. This indicates that $\tilde{R}$ varying is not the correct explanation for the observation.

It is possible that further analysis of $R(t)$ will reveal the relation between reflectivity and incident velocity. However, this pattern of the residuals is also visible in a fit of the above model to classical reflection. The main limitation of the above discussion is the assumption of free propagation of the particle. As a matter of fact, at the reflection point $\tilde{x}$ the particle has doubled its initial kinetic energy. This shows that even though the approximation made describes the data very well, it is not sufficient. The spreading of the wave packet due to a non-constant potential should be taken into account in future work.

3.2.3 Quantum and classical reflection in comparison

Both classical and quantum reflection happen at a physical surface (see full potential in Fig. 1). Therefore, it is conceivable that comparison between a classically and quantum reflected wave packet provides a method to measure the potential, especially the part between quantum and classical reflection point.

The full interaction potential between atom and surface (Eq. (1)) has a well depth of 5.5meV for helium and silver (see [7], p. 3997). This is so deep that our numerical scheme stops working and produces artificial reflections.

Two approaches were used to circumvent this issue and allow usage of the numerical scheme. First, the absorbing boundary was removed from the attractive (parabolically continued) potential. Parts of the wave packet transmitted through the quantum reflection point will then not be absorbed but classically reflected at the left edge of the numeric box.

Since quantum reflection is only a small percentage of classical reflection and the delay is small, quantum reflection is not visible in $R(t)$. Instead, $R(t)$ looks just as discussed above, saturating at $R(t \to \infty) = 1$ because all of the incident wave packet is eventually reflected (classically).

The delay between classical and quantum reflection can be identified by comparing the fit parameters $(\tilde{x} - x_0)$ from simulations with and without absorbing boundary, as shown in Fig. 13.

3.2.4 Experimentally isolating quantum and classical reflection

The second approach is modifying the parameters of the full interaction potential (Eq. (1) and Fig. 1) such that it is considerably less deep. Additionally, in order to increase the delay between quantum and classical reflection, the potential was artificially broadened at the minimum by inserting a constant region.

Despite the modifications to the full interaction potential, results obtained with the modified potential are physically interesting: Since both potentials exhibit the same $-C_3/x^3$ behaviour for large x, they are expected to affect quantum reflection similiarly.

Classical and quantum reflection can indeed be seen separately in sufficiently broad potentials. In fact, multiple reflections as illustrated in Fig. 14 are visible. The reflectivity $R(t)$ (Fig. 15) shows R increasing to one in two steps, first quantum and then classical reflection. Reflected wave functions (Fig. 16) show multiple peaks corresponding to quantum, classical and multiple reflections.

The theoretical possibility of a spin echo experiment showing the delay between quantum and classical reflection arises. A spin echo experiment makes use of an additional degree of freedom, spin, to measure interference [11]. After travelling through a magnetic field, an initial particle with equal spin up and down components will have separate spin up and down packets with a time separation Δt due to their distinct energies in the magnetic field. The interaction with the surface potential is independent of spin. The overlap of the two peaks after reflection in the potential can be measured. By scanning through Δt, the interference of the reflected particle is recovered.

In the present calculation, instead of scanning through Δt, we scan through Δx in the reflected wave function. This is computationally favourable, does not need spin and produces a similar result. Thus, we calculate the interference by cutting out the first two peaks $\psi_{\mathrm{CR}}(x)$ and $\psi_{\mathrm{QR}}(x)$ from $\psi(x, t = 4.8\mu s)$ (see Fig. 16) and applying a delay Δx to the second:

$$\int \psi_{\mathrm{CR}}(x)\psi^*_{\mathrm{QR}}(x + \Delta x)dx. \tag{21}$$

The result can be seen in Fig. 17.

First of all, the peaks of the reflected particle are not at the same position. This leads to the maximum of the interference not being at $\Delta x = 0$. On the other hand, the classically reflected particle has also picked up more phase because it has travelled

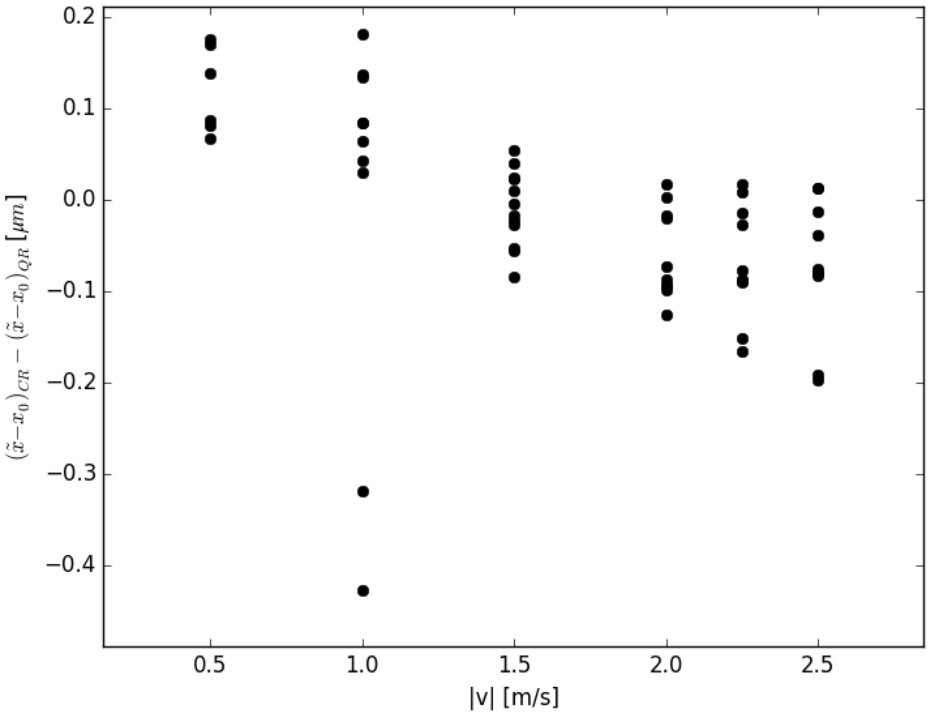

Figure 13: Delay between classical reflection at the boundary of the numeric box (no absorption filter) and quantum reflection (with absorption filter). $(\tilde{x} - x_0)$ is the distance between initial particle and reflection point. The difference $(\tilde{x} - x_0)_{\mathrm{CR}} - (\tilde{x} - x_0)_{\mathrm{QR}}$ is a measure for the spatial distance between classical and quantum reflection points and hence an indication for the expected time delay. Differences of the fit parameters $(\tilde{x} - x_0)$ are plotted for fixed v and multiple parameters $\sigma_0, x_{\mathrm{stop}}$ as in Fig. 10. Note that the delay is negative at larger velocities.

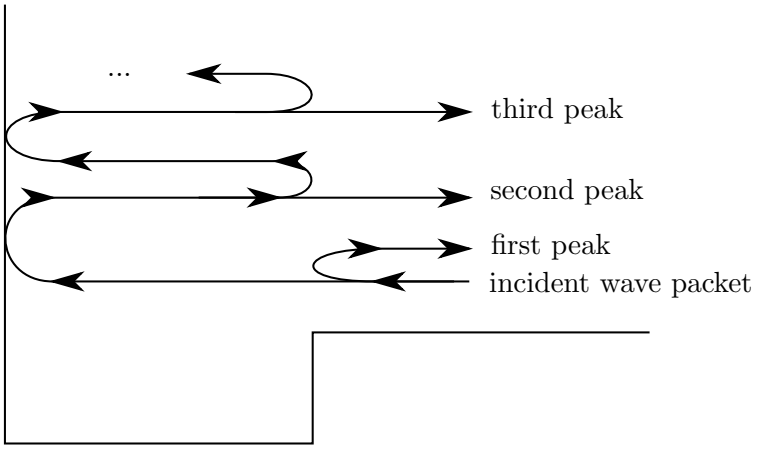

Figure 14: Diagram illustrating multiple reflections occurring in a widened potential. Multiple reflections occurring can be seen in Fig. 15 as $R(t)$ decreasing after the first back-reflection and in Fig. 16 as multiple peaks travelling out of the potential.

further. This leads to a phase shift in the interference. This phase difference could in principle be measured for example in an atomic beam spin echo experiment as described above.

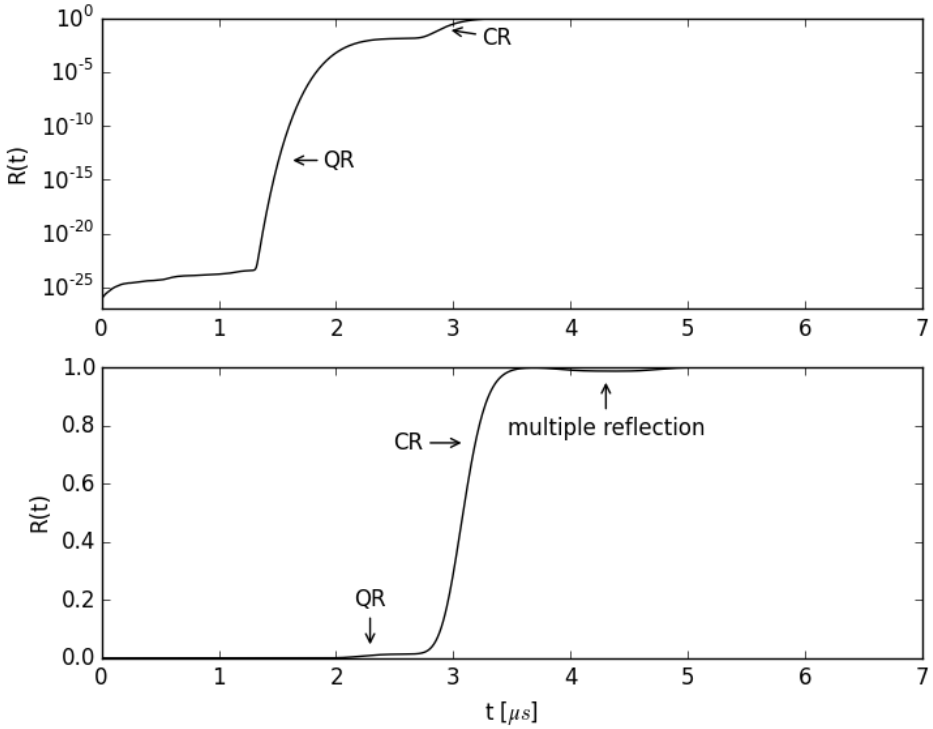

Figure 15: Reflection in a widened potential of a ^{3}He particle with $v = -2$m/s. In the logarithmic scale, quantum reflection and saturation and subsequent classical reflection and saturation to $R(t \to \infty) = 1$ is visible. Moreover, the linear scale also shows multiple reflection that leads to R decreasing again.

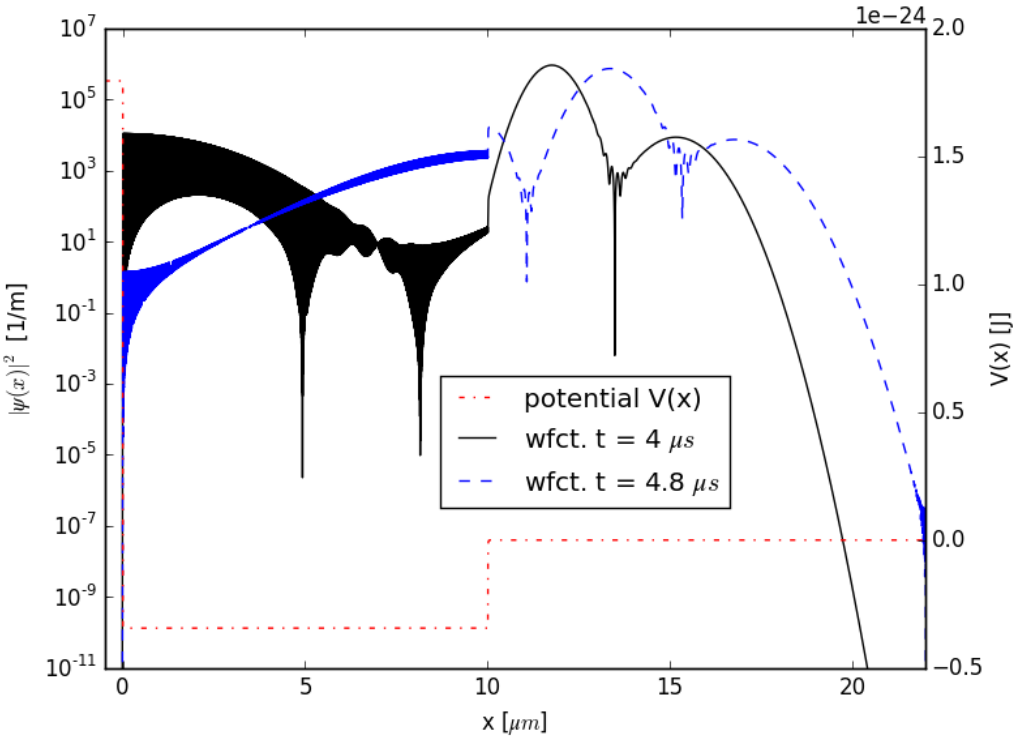

Figure 16: Wave functions after reflection from the widened potential. The broadened potential does not look, but is indeed smooth, which can only be recognised at the relevant length scale of ≈ 1-100nm. A smaller x-scale would be necessary to see this. The wave function at 4μs shows the first two reflection peaks (see Fig. 14) and in the later wave function three reflection peaks become visible. The height of the first peak is significantly lower than that of the second peak, because the probability for quantum reflection is lower than that of classical reflection.

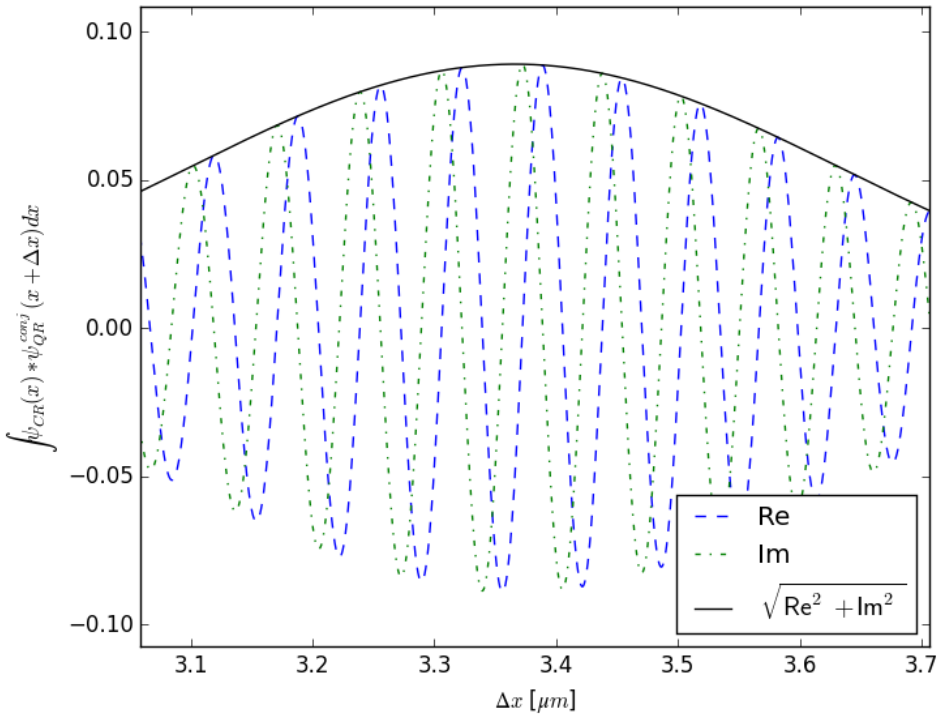

Figure 17: Interference (Eq. (21)) of the first two peaks $\psi_{\mathrm{QR}}(x)$ and $\psi_{\mathrm{CR}}(x)$ cut out of the reflection $\psi(x, t = 4.8\mu\mathrm{s})$ (in Fig. 16). The velocity of the incoming particle was $-2\mathrm{m/s}$. The maximum is not at $\Delta x = 0$. This shows that the two peaks have a certain distance and have not been reflected simultaneously. The phase difference shows the additional phase that has been picked up by the classically reflected particle.

4 Conclusion and Perspectives

A numerical scheme for analysing quantum reflection so far is available only in one dimension (section 2). However, experiments show that one dimension is not sufficient to understand quantum reflection from surfaces. An extension of the scheme to two dimensions was sought (section 3.1.1). It involves computing the LL^t decomposition of a matrix, which should have a bandwidth as low as possible to speed up computations. The minimum bandwidth achievable was determined to be the width m of the numerical $n \times m$ grid (for $n \geq 2m - 1$).

Next, the practical suitability of the two-dimensional scheme was assessed by extrapolating time and memory usage (section 3.1.2). It involves computational costs too high to be of any practical interest for the time being. Thus, explicit methods for integrating the Schrödinger equation could be considered to tackle two-dimensional calculations.

The one-dimensional method was used to study quantum reflection in detail. In particular, it is interesting to look at the time course of reflection and study the swiftness and shape of the reflection process. First, a prominent feature in the time course of reflection could be identified as background resulting from the numeric method used (section 3.2.1).

A model was developed that explains the reflection process well (section 3.2.2). It is based on the approximation that the initial wave packet propagates freely towards the reflection point. Thereafter, the time course of the reflection process is highly dependent on the shape of the initial wave packet. We observe deviations from the model which remain an open question. The changing shape of the wave packet due to propagation in the potential as opposed to free propagation has yet to be considered. Since quantum reflection is non-trivially dependent on velocity, it is expected that a future analysis of the deviations will reveal many details of the process.

When quantum reflection occurs at a surface, classical reflection needs to be considered as well because the surface potential has a repulsive regime. The question whether and how to differentiate between classical and quantum reflection arises naturally. Using the model developed for the time course of quantum reflection, it is shown that classical and quantum reflection at a surface potential show a relative delay dependent on incident particle velocity (section 3.2.3).

Although the numeric approach encountered difficulties with the full interaction potential because of the extremely deep attractive well, results obtained with a modified, broader potential (section 3.2.4) are still interesting to experimentalists. It was shown that in the widened potential, a phase as well as time shift between classically and quantum

reflected particle is visible. The real potential is not as broad, but it is considerably deeper. This means that the acquired phase of the classically reflected particle is significant. Experimentally, this would require a very smooth surface and shallow potentials, since small variations in the attractive part of the potential may lead to large shifts in the acquired phase and to possible decoherence.

References

[1] Th. Gasenzer, *Theoretische Physik IV — Quantenmechanik*, lecture series (2013)

[2] P. L. Garrido, S. Goldstein, J. Lukkarinen, R. Tumulka, *Paradoxical reflection in quantum mechanics*, American Journal of Physics **79**, 1218 (2008)

[3] F. Shimizu, *Specular Reflection of Very Slow Metastable Neon Atoms from a Solid Surface*, Physical Review Letters **86**, 987 (2001)

[4] B. Herwerth, *Dynamics of Quantum Reflection in Atom-Surface Interactions*, Bachelor Thesis (Institute for Theoretical Physics, Heidelberg, 2011)

[5] M. DeKieviet, personal communication (2014)

[6] G. Vidali, G. Ihm, H.Y. Kim, M. Cole, *Potentials of physical adsorption*, Surface Science Reports **12**, 135 (1991)

[7] G. Ihm, M. Cole, F. Toigo, G. Scoles, *Systematic trends in van der Waals interactions: Atom-atom and atom-surface cases*, The Journal of Chemical Physics **87**, 3995 (1987)

[8] B. Herwerth, M. DeKieviet, J. Madroñero, S. Wimberger, *Quantum reflection from an oscillating surface*, Journal of Physics B: Atomic, Molecular and Optical Physics **46**, 141002 (2013)

[9] W. H. Press, S. A. Teukolsky, W. T. Vetterling, B. P. Flannery, *Numerical Recipes*, 3rd ed. (Cambridge University Press, Cambridge, 2007)

[10] B. Fornberg, *Generation of Finite Difference Formulas on Arbitrarily Spaced Grids*, Mathematics of Computation **51**, 699 (1988)

[11] U. Warring, *Auf der Suche nach dem perfekten Quantenreflex*, Diploma Thesis (Physikalisches Institut, Heidelberg, 2006)

[12] E. Cerboneschi, R. Mannella, E. Arimondo, L. Salasnich, *Oscillation frequencies for a Bose condensate in a triaxial magnetic trap*, Physics Letters A **249**, 495 (1998)

[13] E. Jones, T. Oliphant, P. Peterson et al., *SciPy*: Open source scientific tools for python (2001–2014)

[14] Wolfram|Alpha (2014)

Erklärung

Ich versichere, dass ich diese Arbeit selbstständig verfasst und keine anderen als die angegebenen Quellen und Hilfsmittel benutzt habe.

Heidelberg, den 6.10.2014,